

# Terahertz Sources Based on Metrological-Grade Frequency Combs

Elisa Riccardi, Valentino Pistore, Luigi Consolino, Alessia Sorgi, Francesco Cappelli, Roberto Eramo, Paolo De Natale, Lianhe Li, Alexander Giles Davies, Edmund H. Linfield, and Miriam S. Vitiello\*

**Broadband metrological-grade frequency comb (FC) synthesizers with a rich number of phase locked modes are the ideal sources for quantum sensing and quantum metrology. At terahertz (THz) frequencies, electrically pumped quantum cascade lasers (QCLs) have shown quantum-limited frequency noise operation, phase/frequency absolute referencing and self-starting FC operation, albeit over a rather restricted dynamic range, governed by the nature of the quantum gain media that entangles group velocity dispersion at the different bias points. Here, a technological approach is conceived to achieve FC operation over the entire available gain bandwidth at THz frequencies. The intracavity light intensity of a multistack QCL, inherently showing a giant Kerr nonlinearity, is altered by increasing the mirror losses of its Fabry-Perot cavity through coating the back facet with an epitaxially-grown multilayer graphene film. This enables a frequency modulated THz FC showing a proliferation of emitted modes over the entire gain bandwidth and across more than 60% of its operational range, with  $\approx 0.18$  mW per mode optical power. The QCL FC is then experimentally characterized to assess its phase coherence, reconstructing its intensity emission profile, instantaneous frequency, and electric field, thus proving its metrological nature.**

## 1. Introduction

Frequency comb synthesizers (FC) are optical sources emitting a set of discrete, equally spaced and coherent optical modes in the frequency domain, sharing a well-defined phase relation.<sup>[1]</sup> Being inherently narrow linewidth, these light sources allow for absolute frequency measurements throughout the electromagnetic spectrum and have proved to be an appealing technology in quantum science.<sup>[2]</sup> This is especially true in quantum sensing and metrology,<sup>[3,4]</sup> thanks to the resonance with rotational molecular energy levels, and in quantum communication, in view of wireless implementations of quantum key distribution.<sup>[5]</sup>

Widely developed in the visible,<sup>[4]</sup> near-infrared,<sup>[6]</sup> and mid-infrared<sup>[7]</sup> regions of the electromagnetic spectrum, FCs conventionally rely on a chain of optical components, which limits their usability and potential for on-chip integration. The recent observation of spontaneous FC

generation in electrically pumped quantum cascade lasers (QCLs)<sup>[8,9]</sup> has stimulated broad research efforts in the development of chip-scale FCs operating in the still mostly unused terahertz (THz) frequency range, which is strategic for future quantum applications.<sup>[2]</sup>


Unlike conventional FCs that rely on the emission of short pulses from mode locked sources, QCL combs produce a generally frequency-modulated (FM) output with an almost constant intensity and a linear frequency chirp,<sup>[10]</sup> due to the large nonlinear susceptibility of the semiconductor heterostructure gain medium. At THz frequencies (2–5 THz), frequency and amplitude modulation act simultaneously<sup>[11–13]</sup> as an effect of the four wave mixing process generated by either fast saturable gain,<sup>[10]</sup> which controls the frequency modulation, or by loss,<sup>[9,13]</sup> which governs amplitude modulation. However, in a free-running THz QCL, the FC regime is self-starting only in specific operational regimes in which the group velocity dispersion<sup>[14–16]</sup> is low enough to allow the cavity modes to be locked by the modes generated by the intracavity four-wave-mixing process,<sup>[9]</sup> without requiring any additional optical element.

Adapting the bias-dependent contribution to the chromatic dispersion while preserving and enhancing the optical

E. Riccardi, V. Pistore, M. S. Vitiello  
CNR-Istituto Nanoscienze and Scuola Normale Superiore  
NEST  
Piazza San Silvestro 12, Pisa 56127, Italy  
E-mail: miriam.vitiello@sns.it

L. Consolino, A. Sorgi, F. Cappelli, R. Eramo, P. De Natale  
CNR-Istituto Nazionale di Ottica and European Laboratory for Non  
Linear Spectroscopy  
Sesto Fiorentino 50019, Italy

L. Li, A. G. Davies, E. H. Linfield  
School of Electronic and Electrical Engineering  
University of Leeds  
Leeds LS2 9JT, UK

 The ORCID identification number(s) for the author(s) of this article can be found under <https://doi.org/10.1002/lpor.202200412>

© 2022 The Authors. Laser & Photonics Reviews published by Wiley-VCH GmbH. This is an open access article under the terms of the Creative Commons Attribution-NonCommercial-NoDerivs License, which permits use and distribution in any medium, provided the original work is properly cited, the use is non-commercial and no modifications or adaptations are made.

DOI: 10.1002/lpor.202200412

bandwidth is therefore essential to achieve a reliable control of the comb states across the whole operational range. While gain medium engineering proved to be a suitable solution to optimize the optical bandwidth, it severely influences the dispersion dynamics at the different bias points. The most commonly adopted strategies to compensate this latter effect include intracavity-integrated dispersion compensators<sup>[9,17]</sup> or Gires–Tournois etalons. These comprise a planar mirror,<sup>[18,19]</sup> a graphene modulator,<sup>[20]</sup> or a saturable absorber graphene reflector,<sup>[21]</sup> individually placed behind the laser facet to induce a wavelength dependent group delay, providing stable FC operation over 29%–55% of the laser operational range.<sup>[9,19–22]</sup> Alternatively, dc-biased external cavity sections can induce FC operation over the whole QCL bias range but with a rather limited optical bandwidth (0.4 THz).<sup>[23]</sup>

However, recent theoretical work<sup>[24]</sup> has shown that full dispersion compensation does not necessarily lead to comb spectra covering the entire available gain bandwidth or across the whole lasing regime and has shed light on the key role of the multiple effects governing stable FC operation in a QCL. Due to the ultrafast gain recovery time (50 ps in a heterogeneous structure)<sup>[25]</sup> of QCLs, the spectral gain asymmetry due to Bloch gain yields to a giant Kerr nonlinearity (of the order  $10^{-15} \text{ m}^2 \text{ W}^{-1}$ )<sup>[26–29]</sup> that acts as a resonant nonlinear effect that tends to alter FC operation.<sup>[27]</sup> The Kerr effect, together with the intracavity light intensity profile,<sup>[30]</sup> plays a dominant role in the formation of frequency-modulated combs.<sup>[24,27,31–33]</sup> However, while the Kerr nonlinearity is an inherent feature of the gain media architecture, the intracavity light intensity profile can be controlled and tuned technologically.

Here, we alter the intracavity light intensity in a heterogeneous terahertz QCL FC with a 1.3 THz bandwidth, by reducing the reflectivity of the back QCL facet to induce higher mirror losses. In a Fabry–Perot laser cavity, the intensities of the propagating and counterpropagating components of the electromagnetic intracavity field increase as they propagate, since the facets are semitransparent.

The slope of the intensity with respect to the propagation distance has a crucial impact on the comb operation due to cross-steepening,<sup>[32]</sup> i.e., a group delay term dependent on the intensity of the counter propagating waves. This last term is significant only when there is a large change in the intracavity power at a facet, i.e., large mirror losses. After reflection from a facet, which induces a significant power discontinuity for sufficiently large mirror losses, the wave experiences positive feedback of its phase as it sees its phase at an earlier time in the counter-propagating wave. Comb operation can consequently be altered by changing the coatings of the laser facets. This, in turn, locally alters the refractive index of the medium. This picture, supported by the theoretical framework of refs. [24, 31, 32], is the expected mechanism for the spectral broadening and stabilization achieved in the present work.

To this purpose, we lithographically cover the laser back facet with a multilayer (seven layers) graphene film (MLG) grown by chemical vapor deposition (CVD). A proliferation of the emitted modes over a 1.3 THz bandwidth and across 60% of the laser operational range is achieved. In this configuration, the modal phases of the QCL FC are retrieved, in order to assess its phase coherence and to reconstruct its in-

tensity emission profile, instantaneous frequency, and electric field.

## 2. Results and Discussion

### 2.1. Device Architecture

The structure employed in the present work is a 17  $\mu\text{m}$  thick GaAs/AlGaAs heterostructure comprising three active modules, with comparable threshold current densities ( $J_{\text{th}}$ ), all based on longitudinal optical phonon-assisted interminiband transitions,<sup>[34]</sup> and with gain bandwidths centered at 2.5, 3, and 3.5 THz (see the Experimental Section). Fabry–Perot laser cavities in a double-metal waveguide configuration are lithographically defined and employ a 3  $\mu\text{m}$  wide lossy side absorber on the top laser surface aligned along the waveguide edges (see the Experimental Section). The resulting heterogeneous QCL comb has a dynamic range  $J_{\text{max}}/J_{\text{th}} = 3.3$ , where  $J_{\text{max}}$  is the maximum current density at which the QCL show lasing, and a stable FC operation over 13% of its operation range in general agreement with previous reports<sup>[35]</sup> on a similar gain media design. A CVD MLG film is then transferred, following the procedure described in the Experimental Section, onto the facet of a Fabry–Perot laser cavity having the same active region design and the same dimensions (70  $\mu\text{m} \times 2.4 \text{ mm}$ ) of the reference QCL FC. The two devices are electrically and optical tested for comparison. **Figure 1a** shows a scanning electron microscope image of the QCL FC ridge (left) and its graphene-coated back facet (right).

A 0.8 mm  $\times$  0.8 mm square of the same CVD MLG is also transferred onto an undoped GaAs substrate for optical characterization. The MLG optical properties are initially assessed by performing transmission experiments in a compact and purged THz time-domain spectroscopy (TDS) system (Tera K5 by MenloSystems), allowing retrieval of the optical conductivity through the Tinkham formula<sup>[36]</sup> (see Supporting Information). The complex refractive index, extracted over the 0.4–2.2 THz range, is then calculated and extrapolated to higher frequencies as shown in **Figure 1b**. The waveguide of the typical Fabry–Perot THz QCL confines the radiation in a subwavelength volume (typical waveguide thickness of  $\approx 10$ –15  $\mu\text{m}$  compared to a 100  $\mu\text{m}$  wavelength at 3 THz), leading to an impedance mismatch at the facet that significantly increases the reflectivity compared to the value predicted by the Fresnel formula.<sup>[37,38]</sup>

3D simulations (Comsol Multiphysics) are performed (see Supporting Information) to evaluate the effect of the MLG coating on the QCL facet, modeling it according to the optical parameters extracted from the TDS measurements. **Figure 1b** displays the facet reflectance with (red curve) and without (black curve) the MLG coating in the 2.5–3.7 THz range. A significant (22% to 33%) reduction of the facet reflectance is observed when the graphene is present, demonstrating that the MLG acts as an antireflection coating for the THz radiation. It is also consistent with the theoretical background developed in ref. [39] for nanometers-thick layers of materials with a high imaginary part of the refractive index at THz frequencies such as graphene. These conditions could also be met, in principle, by employing some low reflectivity dielectric films. Dielectrics such as parylene<sup>[40]</sup> and  $\text{SiO}_2$ <sup>[41]</sup> have indeed been shown to suppress reflection from single-plasmon THz QCL facets

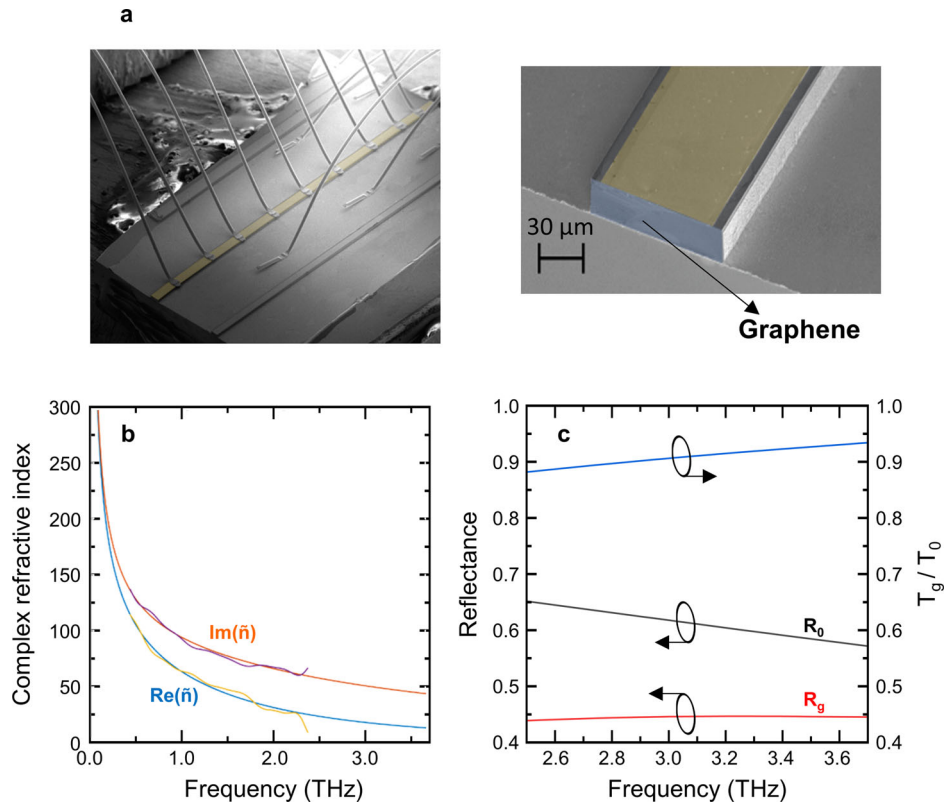


**Figure 1.** MLG coated QCL scanning electron microscopy (SEM) imaging and MLG optical properties simulation. a) False color scanning electron microscope images of a graphene-coated Fabry–Perot QCL double metal cavity (left) and back facet coated with multilayer graphene (MLG) (right). The MLG on the back facet is indicated in light blue. b) Complex refractive index of the MLG extracted from THz-TDS transmittance measurements. The purple and yellow curves correspond to the experimental imaginary and real part of the refractive index, while the orange and blue curves are fit corresponding to DC conductivity  $\sigma_{DC} = 1.72$  mS and scattering time  $\tau = 68$  fs. c) Left vertical axis: facet reflectance spectrum of the pristine QCL ( $R_0$ , black curve) and of the QCL with the graphene coating ( $R_g$ , red curve) from 3D COMSOL simulations. The graphene optical parameters employed in the simulation are the same as panel b. Right vertical axis: Simulated transmittance spectrum of the THz radiation through the MLG coated facet (blue curve), normalized to the transmittance of the uncoated facet, which is theoretically given by  $T_0 = 1 - R_0$  and validated by simulations.

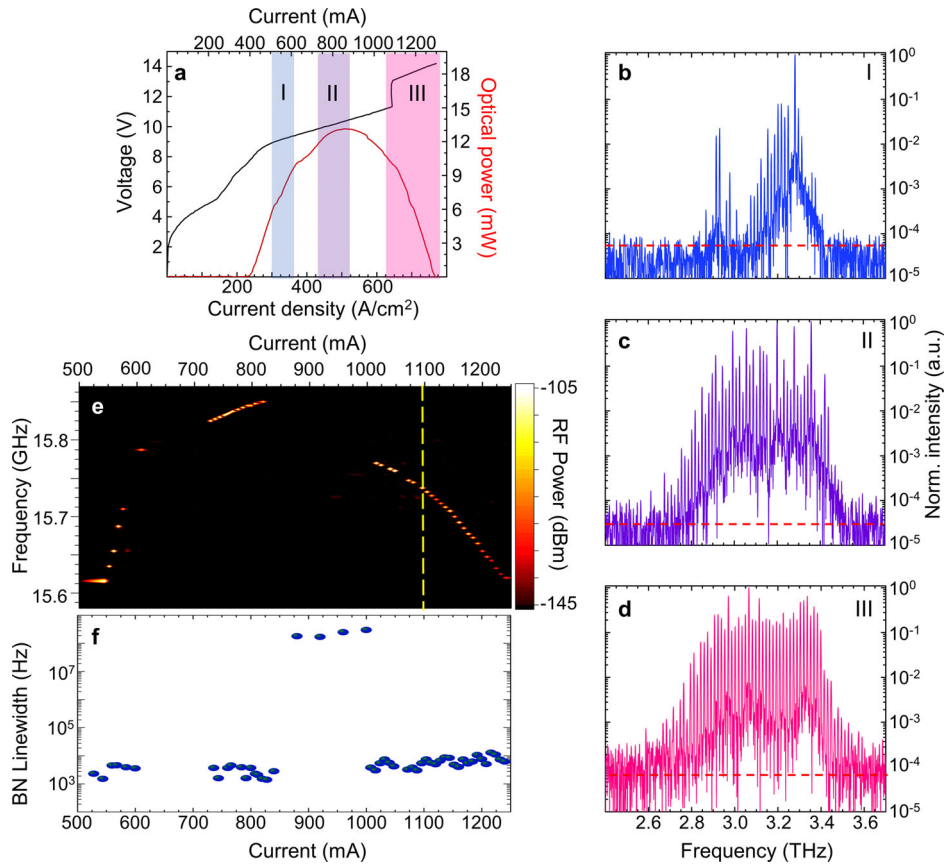
according to a design based on the effective index method, i.e., employing the Fresnel reflection coefficients.<sup>[40,41]</sup> However, this approach cannot be extended to double-metal waveguides due to the impedance mismatch caused by the strong subwavelength confinement of the radiation in the laser cavity.<sup>[38]</sup> Furthermore, the choice of the dielectric must be compatible with a deposition thickness larger than  $10 \mu\text{m}$ .<sup>[40]</sup> Gires–Tournois interferometric effects affecting the device dispersion<sup>[17]</sup> may even need to be accounted for when employing dielectric layers of such thicknesses.

Figure S1a in the Supporting Information shows the QCL facet reflectance spectrum as a function of the imaginary part of the MLG refractive index. Whereas a reduction of the facet reflectance is always observed, one can tune this reduction by changing, e.g., the MLG Fermi level or doping concentration, which affect the optical properties of the graphene,<sup>[42]</sup> or the number of graphene layers (Figure S3, Supporting Information). Nonlinear effects associated with the strong graphene nonlinearity in the THz regime ( $\chi^{(3)} \approx 10^{-9} \text{ m}^2 \text{ V}^{-2}$ )<sup>[43]</sup> are considered (see Supporting Information) by evaluating the electric field response to the change of the MLG optical properties, such as a reduction of the imaginary part of the MLG refractive index associated with saturable absorption phenomena. As shown in a recent work,<sup>[24]</sup> a reduction of the facet reflectivity in conjunction with a suffi-

ciently strong Kerr nonlinearity can enhance the phase locking of the QCL modes while simultaneously increasing the number of optically active phase-locked modes. The transmittance of the MLG-coated facet is also reduced by 10–15% due to the absorption of the graphene (Figure 1c, blue curve).

## 2.2. Electrical Transport and Optical Characteristics

Continuous-wave (CW) current–voltage ( $I$ – $V$ ) and light–current ( $L$ – $I$ ) characteristics (Figure 2a) show that the FC delivers a maximum optical power that is 17% lower than that collected on the back facet of an uncoated QCL (Figure 3a) and reaches 13 mW at the peak, with a slope efficiency of  $52 \text{ mW A}^{-1}$ . Therefore, it is 25% larger than that of the uncoated QCL (Figure 3a). We observe a maximum wall-plug efficiency of 0.14%, 10% lower than the corresponding value of the uncoated laser (Figure 3a). The device shows a dynamic range  $J_{\text{max}}/J_{\text{th}} = 3.3$  (Figure 2e) with a threshold current density  $J_{\text{th}} = 237 \text{ mA cm}^{-2}$ , 6% higher than the uncoated reference device (Figure 3a). Such a performance change is as an effect of the increased mirror losses  $\alpha_m$ , induced by the graphene coating. A statistical analysis of the key figure of merits in a set of different graphene coated and uncoated



**Figure 2.** Electric and optical characterization of the MLG-coated comb device. a) Voltage–current density ( $V$ – $J$ ) and light–current density ( $L$ – $J$ ) characteristics measured in continuous wave, at 20 K. The shaded areas (light blue, purple and pink) indicate the three bias regimes in which the QCL operates as a frequency comb. The optical power has been measured using a broad-area terahertz absolute power meter (thomas keating (TK) Instruments, aperture  $55 \times 40 \text{ mm}^2$ ). b–d) Fourier transform infrared (FTIR) spectra collected in rapid scan mode under vacuum, with a  $0.075 \text{ cm}^{-1}$  resolution at 20 K, while driving the QCL in continuous wave at b) 550 mA, c) 800 mA, and d) 1100 mA, corresponding to the three shaded area in the  $J$ – $V$  characteristic of panel (a). The dashed lines mark the noise level. e) Intermode beatnote map and f) linewidths, plotted as a function of the QCL driving current, measured at 20 K. The dashed yellow line indicates the point at which the metrological characterization has been performed.

QCLs is reported in the Supporting Information. From the simulations of Figure 1b,c we estimate the ratio between the mirror losses of the QCL with ( $\alpha_{\text{m}(\text{graphene})}$ ), and without ( $\alpha_{\text{m}(\text{pristine})}$ ), the graphene-coated facet  $\frac{\alpha_{\text{m}(\text{graphene})}}{\alpha_{\text{m}(\text{pristine})}} = 1.46$ . By assuming waveguide losses of  $6 \text{ cm}^{-1}$ ,<sup>[44]</sup> the slope efficiency  $dP_0/dI = \eta_{\text{int}} \alpha_{\text{m}} / \alpha_{\text{tot}} N h \nu / e$  (where  $\alpha_{\text{tot}}$  is the total losses,  $N$  is the number of stages in the active region,  $\eta_{\text{int}}$  is the injection efficiency,  $h \nu$  the photon energy, and  $e$  the electron charge), the wall plug efficiency is  $\eta_{\text{ini}} (\alpha_{\text{m}} / \alpha_{\text{tot}}) (N h \nu / e) (1/V) [1 - (J_{\text{th}}/J)]$  (where  $V$  is the operational bias), and the threshold current density  $J_{\text{th}} = \alpha_{\text{tot}} / g \Gamma$  (where  $g \Gamma$  is the product of material gain and the confinement factor), we expect by increasing the mirror loss through introduction of the MLG coating, a 31% increase in slope efficiency, a 10% increase in  $J_{\text{th}}$ , and a reduction of the maximum wall plug efficiency of 17%, in general agreement with those values observed experimentally. The slight discrepancy, in agreement with the measured standard deviation in a wide set of tested devices (Figure S7, Supporting Information), results from considering only the change in the facet reflectivity, without including any possible saturation effect of the MLG absorption.

Representative CW Fourier transform infrared spectra (Figure 2b–e), measured under vacuum and at different driving currents (550, 800, and 1100 mA), show that the spectra gradually broaden as the bias current is increased, spanning a spectral range of 0.6 THz, just above threshold, and 1.3 THz (2.4–3.7 THz) with an optical power of  $\approx 0.18 \text{ mW}$  per mode at the onset of the negative differential resistance regime, where QCLs usually become intrinsically unstable due to high field domain formation.

Figure 2e shows the corresponding free running electrical intermode beatnote (IBN) map. The latter typically provides a genuine indication of the coherence properties of the emitted modes of a QCL-based frequency comb.<sup>[8]</sup> Beatnote signals are extracted from the bias line, using a bias-tee, and recorded with a radio frequency (RF) spectrum analyzer (Rohde and Schwarz FSW43). A single and narrow (2–8 kHz) intermode beatnote, the signature of a genuine and stable comb regime, is recorded in the three different transport regimes identified by shaded areas in Figure 2a and covering almost 60% of the operating bias range: i) for 100 mA above the onset of resonant injection into the upper state (region I); ii) around the peak optical power (700–850 mA); and iii) for

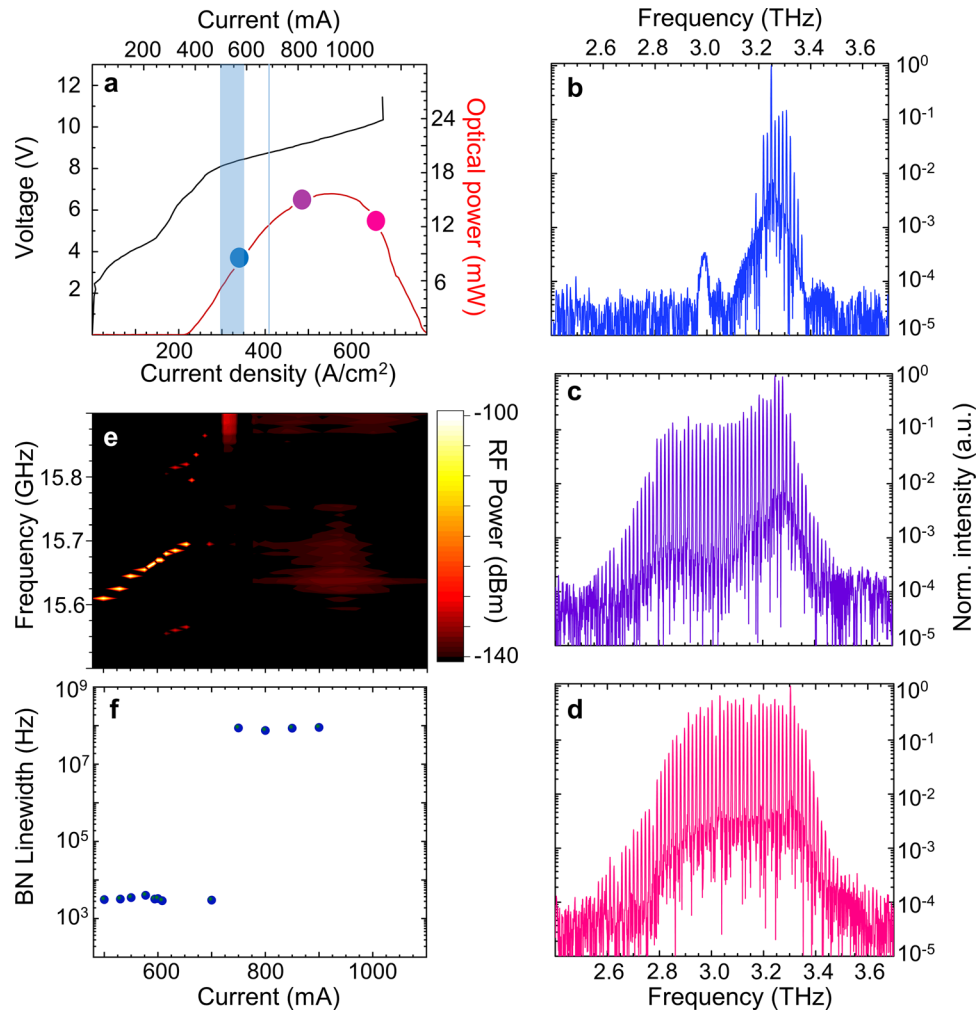


**Figure 3.** Electric and optical characterization of the uncoated QCL. a) Voltage–current density ( $V$ – $J$ ) and light–current density ( $L$ – $J$ ) characteristics measured in continuous wave, at 20 K for a  $70\ \mu\text{m} \times 2.4\ \text{mm}$  QCL. The optical power has been measured using a broad-area terahertz absolute power meter (TK Instruments, aperture  $55 \times 40\ \text{mm}^2$ ). The shaded area and shaded thin line identifies the regime in which the QCL behaves as a comb. b–d) FTIR emission spectra collected in rapid scan mode, under vacuum with a  $0.075\ \text{cm}^{-1}$  resolution at 20 K, while driving the QCL in continuous wave at 550 mA b) where the QCL operates as frequency comb, c) 800 mA and d) 1100 mA, corresponding to the three circle in the  $J$ – $V$  characteristic of panel (a). e) Intermode beatnote map plotted as a function of the QCL driving current. f) Intermode beatnote linewidths plotted as a function of the QCL driving current, measured at 20 K.

almost 250 mA across the negative differential resistance regime (region III,  $>1\ \text{A}$ ), where the beatnote linewidth slightly increases from the 2–6 kHz value retrieved in regions I and II to values of 3–10 kHz. Such a behavior differs significantly from that observed in the uncoated QCL (Figure 3e,f). In this latter case, a stable FC regime is only found in region I, i.e., for 100 mA above the onset for resonant injection.

It is worth mentioning that graphene can also potentially introduce intensity dependent losses into the external laser cavity.<sup>[45,46]</sup> Reflection on the graphene surface contributes to frequency comb stabilization through the same mechanism as the fast saturable gain in the QCL active region, forcing the QCL into frequency-modulated operation. Saturable absorption phenomena, experimentally observed in MLG films,<sup>[46]</sup> could also help to regularize the remaining amplitude modulation that can combine with the dominant frequency modulation effect.<sup>[21]</sup>

However, the contribution of the saturable losses to the total losses has been observed to increase with the number of layers in the MLG,<sup>[47]</sup> hence making nonlinear phenomena in our MLG coating of negligible relevance.

### 2.3. Metrological Characterization

To further corroborate our claims, we perform a metrological-grade analysis of our FC emission.

To this purpose, we evaluate the overall phase coherence of the FC when it reaches the maximum spectral coverage and mode proliferation (1.1 A) by the Fourier Analysis of Comb Emission (FACE) technique.<sup>[12,48]</sup> This technique gives access to the Fourier phase information of the QCL comb modes, which ultimately determine the comb behavior of the device. It is based

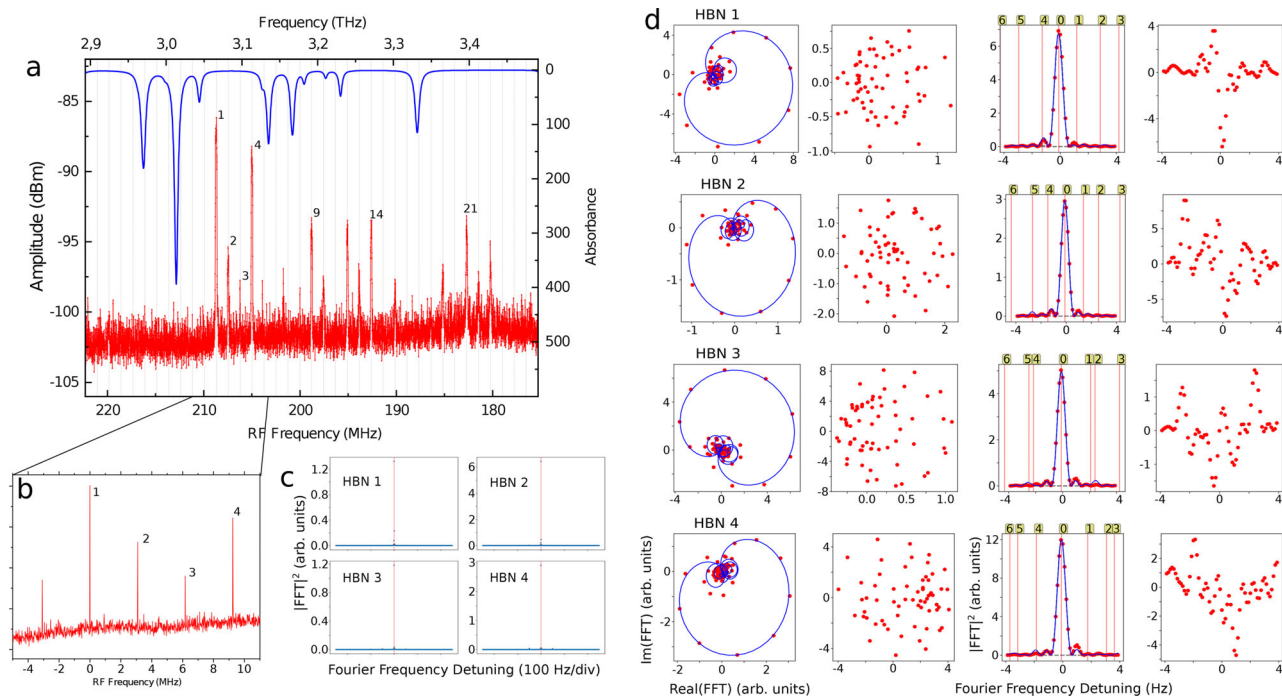


**Figure 4.** Down-conversion and phase stability assessment. a) fast Fourier transform (FFT) amplitude spectrum of the down-converted radio frequency comb (RF-FC, red trace) acquired from the fast mixer (hot-electron bolometer). The heterodyne beatnotes (HBNs) are conveniently numbered for reference, while gray vertical lines predict the position of all the possible comb modes. Retrieval of the absolute frequency of all the modes with high accuracy (see Supporting Information) allows a direct comparison with the water vapor absorption spectrum (blue trace). b) Acquisition of the RF-FC with excess frequency noise rejection. The local oscillator frequency comb (LO-FC) is a zero-offset comb and its repetition rate is phase stabilized to a global positioning system (GPS) ruled Rb-quartz chain ( $2 \times 10^{-12}$  accuracy). The sample QCL frequency comb has injection locked mode spacing, while the common mode noise is electronically subtracted. The resulting amplitude spectrum, acquired with a spectrum analyzer, is resolution bandwidth limited (RBW = 100 Hz). The frequency of HBN1 is artificially shifted to zero. c) The RF-FC signal is acquired as a time trace in quadrature (I and Q), in a 1.3 s long acquisitions. The resulting FFT spectra (blue traces) confirm that the HBNs have a sub-Hz width, indicating a high level of coherence and stability in the QCL FC. A total of 39 modes emitted by the QCL comb are retrieved in these acquisitions, covering a spectral range of more than 600 GHz. d) The real and imaginary part of the discrete Fourier transform (DFT) spectra of the modes, resampled around each modal frequency employing the Goertzel algorithm, are shown (left), together with the fit and fit residuals. The square modules of the DFT are also shown (right), fitted with seven independent oscillators (blue traces). The central frequency of the main (0) and of the satellites oscillators (1, ..., 6) are also indicated in the graph by a vertical red line, while fit residuals are shown on the right of each panel.

on a multi-heterodyne down-conversion process, relying on the fast mixing of the devised graphene-coated QCL FC sample with a well-known and phase characterized local oscillator frequency comb (LO-FC) obtained by optical rectification of femtosecond mode-locked pulses in a nonlinear crystal. A portion of the obtained down-converted radio frequency comb (RF-FC) is shown in **Figure 4a** (red trace), where the heterodyne beatnotes (HBN) have been conveniently numbered. The absolute frequency of the heterodyne beatnote HBN1 (**Figure 4a**) is determined with the technique described in ref. [49] (see Supporting Information), and by simultaneously acquiring the HBN frequency, from which we ascertain the absolute frequencies of all the modes. The collected traces agree with the FTIR spectra (**Figure 2d**) but the much higher accuracy allows us to compare the QCL emission window with the absorption spectrum of water vapor contained in laboratory air, simulated with Spectraplot, based on the high resolution transmission molecular absorption database (HITRAN) database (**Figure 4a** blue trace). It can be seen that some of the optical modes, especially from the lower-power LO-FC, are strongly attenuated by water vapor along the 2 m optical path up to the fast mixer.

In order to access the Fourier phases of the QCL comb modes, the excess frequency noise on both the QCL FC degrees of freedom (mode spacing and frequency offset) needs to be reduced. To this purpose, a radio frequency signal (20 dB amplitude) close to the QCL cavity round trip time (HBN  $\approx 15.73$  GHz) is sent to the device by a bias tee mounted in the driving current feeding line, and used to injection lock the QCL comb mode spacing.<sup>[48]</sup> Simultaneously, the common-mode noise is eliminated from the RF-FC by means of an electronic chain, as described in ref. [12]. The RF-FC frequency noise is then strongly attenuated and its spectrum appears resolution bandwidth (RBW) limited at 100 Hz (**Figure 4b**). The RF-FC signal is then acquired as a time trace in two quadratures (I and Q) with a 200 MS  $s^{-1}$  sampling rate spectrum analyzer. The acquisition time length is 1.3 s, which results in 1 Hz RBW-limited signals retrieved with an FFT routine (**Figure 4c**). In these experimental conditions, a total of 39 well-defined QCL oscillators could be detected (see **Figure S4**, Supporting Information) covering an optical bandwidth  $>0.6$  THz. Lower intensity peaks retrieved in the FTIR spectrum (**Figure 2**) are missing due the inherently higher sensitivity of the under-vacuum FTIR. This confirms that the

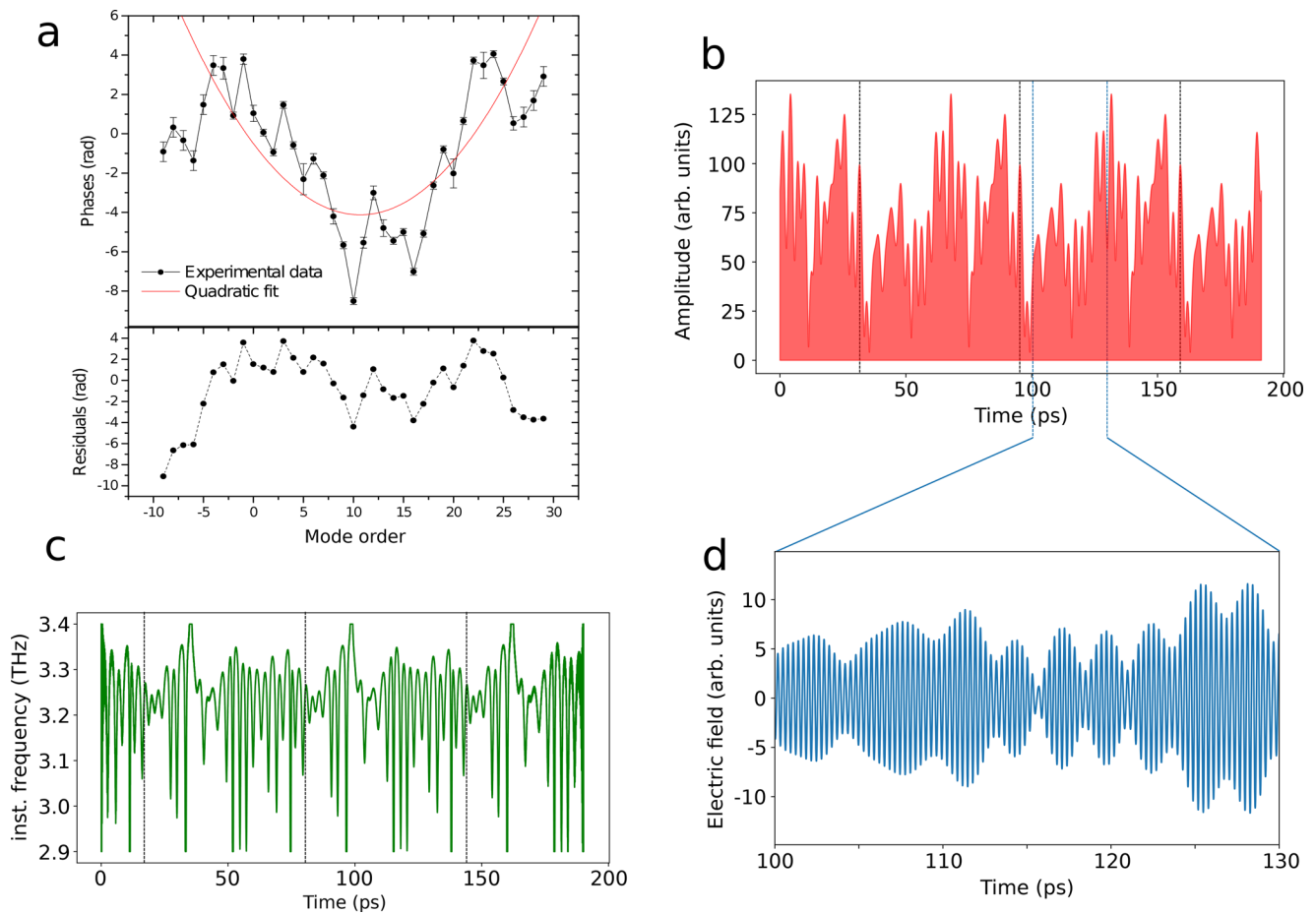


**Figure 5.** QCL frequency comb emission. a) Measured Fourier phases of each mode of the QCL comb, calculated by the fit routines presented in Figure 4d. Parabolic fit of the data is shown, resulting in a measured GDD of  $(3.25 \pm 0.5) \text{ ps}^2 \text{ rad}^{-1}$ . b) Reconstruction of the THz QCL comb output intensity, based on the data shown in panel (a). Despite the clear presence of amplitude modulation, the QCL emission is far from a pulse-like shape and the device is emitting radiation during 48% of the total time. c, QCL comb instantaneous frequency, calculated from the Hilbert transform of the electric field. The total spectral coverage and the fast modulation confirm a substantial FM in the QCL comb emission. d) Detail of the QCL comb emitted electric field.

QCL device behaves as a metrological-grade FC in the explored time scale.

Previous reports of the FACE technique<sup>[12,48]</sup> only took into consideration data in the shape of Figure 4c, where the modal phases were simply extracted by retrieving the phases of the points relative to the amplitude maxima in the FFT spectrum. Here, we follow, for the first time, a different and improved procedure for the data analysis, with a sound theoretical background.<sup>[50]</sup> The spectra have been calculated around each modal frequency by using the Goertzel algorithm.<sup>[51]</sup> The resulting high-resolution discrete Fourier transform (DFT) spectra are then fitted with seven different and independent oscillators. Examples of this procedure are shown in Figure 4d (left), where the real and imaginary part of the DFT spectra of the signals are shown, together with the relative fit. For a better understanding, the square modules are also shown in figure 4d (right), while the complete set of 39 oscillators are reported in the Supporting Information. The modal phases and amplitudes are retrieved from the main oscillator in the fit and are used for the following analysis. The modal phases show a parabolic trend, evidenced by

the nonlinear fit (Figure 5a), which corresponds to a group delay dispersion (GDD) of  $3.25 \pm 0.5 \text{ ps}^2 \text{ rad}^{-1}$ . This value is one order-of-magnitude smaller than the one that is expected for maximally chirped operation ( $\approx 17 \text{ ps}^2 \text{ rad}^{-1}$ )<sup>[52]</sup> and a factor of 2 lower than found in pristine self-starting QCL FCs,<sup>[12,48]</sup> albeit just above threshold, hence in a completely different operating condition. In fact, the MLG coating allows an efficient phase locking of the modes in the regime in which the QCL would be naturally dominated by dispersion<sup>[53]</sup> and likely FC operation would not be possible. This confirms the efficacy of the adopted approach and that the combination of huge Kerr nonlinearity with an altered intracavity intensity can allow phase locking of the modes over the entire gain bandwidth. Moreover, the fit residuals (Figure 5a) cover a phase range of several radians, a condition that is compatible neither with short pulse emission nor with a pulse recompression.

The retrieved modal phases and amplitudes allow the reconstruction of the intensity emission profile (Figure 5b), the instantaneous frequency (Figure 5c), and the electric field (Figure 5d) of the FC. Although the emission profile appears

amplitude modulated, it is far from a pulse-like emission profile as the device emits radiation during  $\approx 48\%$  of the round-trip time, and is mostly affected by temporal hole burning.<sup>[11]</sup> Importantly, the profile of the instantaneous frequency of the emitted field, displayed in Figure 5c, covers the entire emission spectrum of the QCL and oscillates with a dynamics much faster than that observed in QCL combs with no graphene coating,<sup>[12,48]</sup> showing numerous oscillations during the round trip time. This confirms a dominant frequency modulated regime and corroborate the theoretical predictions of ref. [23].

The inherent resonant Kerr nonlinearity of the QCL active region does not compensate for the group velocity dispersion (GVD) alone. In fact, shaping the intracavity field by altering the facet reflectivity helps in broadening the FC emission and in reaching the long-term stability, demonstrated in the present work. This classifies the quantum device presented here as a powerful metrological-grade source in the far-infrared, with potential for scalable incorporation into integrated quantum networks at terahertz and millimeter wave<sup>[54]</sup> frequencies.

### 3. Experimental Section

**Active Region Design:** The individual active regions consist of nine GaAs quantum wells, forming a cascade of alternating photon and LO-phonon-assisted transitions between two quasi-minibands.<sup>[34]</sup> The layer sequences of the three active regions designs are: 10.6/**0.5**/17/1/13.5/2.1/12.4/**3.1**/10/3.1/9/2.9/7.5/3.1/17.8/**3.1**/15.2/4.1;9.8/**0.5**/15.7/1/12.5/2/11.4/**2.9**/9.2/2.9/8.3/2.9/6.9/2.9/16.5/2.9/14.1/3.9;and10.5/**0.5**/12.2/1/12.5/1.9/11/2.8/8.8/2.8/7.9/2.8/6.6/2.8/15.8/**2.8**/13.8/3.7, respectively, where the thickness is in nanometers, the bold figures represent the AlGaAs barriers, and the underlined figures denote the Si-doped ( $3.5 \times 10^{16} \text{ cm}^{-3}$ ) GaAs layer. The aluminum content in the barriers is 0.14, 0.16, and 0.18, respectively.

**QCL Fabrication:** Fabry–Perot laser bars are fabricated in a metal–metal waveguide configuration via Au–Au thermocompression wafer bonding of the 17  $\mu\text{m}$  thick active region (sample L1494) onto a highly doped GaAs substrate, followed by the removal, through a combination of mechanical lapping and wet etching, of the host GaAs substrate of the molecular beam epitaxial material. The  $\text{Al}_{0.5}\text{Ga}_{0.5}\text{As}$  etch stop layer is then removed using hydrogen fluoride (HF) etching. Vertical sidewalls are defined by inductively coupled plasma etching of the laser bars to provide uniform current injection. A Cr/Au (10  $\mu\text{m}$ /150  $\mu\text{m}$ ) top contact is then deposited along the center of the ridge surface, leaving a thin region uncovered along the ridge edges. 3  $\mu\text{m}$  wide Ni (5 nm thick) side absorbers were then deposited over the uncovered region using a combination of optical lithography and thermal evaporation. These lossy side absorbers are intended to inhibit lasing of the higher order lateral modes by increasing their threshold gain.<sup>[55]</sup> Finally, the backside of the substrate is lapped down to 150  $\mu\text{m}$  to allow a proper thermal management and enable operation in CW. Laser bars, 70  $\mu\text{m}$  wide and 2.4 mm long, are then cleaved and ready for the graphene transfer.

**Graphene Transfer:** The multilayer graphene sample is prepared and transferred on the laser facet, using a wet transfer technique. A 4–950 K ply (methyl-methacrylate) polymer (PMMA) is spin coated at 2000 rpm on the surface of a single layer (SLG) sample (1 cm  $\times$  1 cm) grown on Cu via CVD, commercially available by Graphenea Inc. After 1 min on the hot plate at 90  $^{\circ}\text{C}$ , the sample is placed on a solution of 1 g of ammonium persulfate and 40 mL of deionized water (DI) water to etch the Cu substrate. Once the Cu etching is complete, the PMMA–SLG film is transferred in a beaker with DI water and then lifted with a second Cu–graphene square to obtain a bilayer graphene sample. This sample is left dry overnight and finally the PMMA is removed with acetone. The Cu of the bilayer graphene is etched with the same technique, and then lifted by another SLG on Cu. This process is repeated until reached the desired MLG thickness, in the

case seven layers. A small part of the MLG is finally cut, etched, and then lifted with the just cleaved facet of the QCL. To avoid electrical short circuit, the MLG is mechanically removed from the top and side of the ridge by using the micrometric gold wire of the wire bonder machine. Finally, the device is mounted on a copper bar, wire bonded, and then mounted onto the cold finger of a He continuous-flow cryostat.

### Supporting Information

Supporting Information is available from the Wiley Online Library or from the author.

### Acknowledgements

This work was supported by the European Research Council through the ERC Consolidator Grant (681379) Ultrashort pulse laser resonators in the Terahertz (SPRINT), by the European Union through the H2020-FET OPEN EXTREME IR (964735), and by the Engineering and Physical Sciences Research Council (EPSRC) (UK) programme grant “HyperTerahertz” (EP/P021859/1).

Open access funding provided by Consiglio Nazionale delle Ricerche within the CRUI-CARE Agreement.

### Conflict of Interest

The authors declare no conflict of interest.

### Author Contributions

E.R. and L.C. contributed equally to this work. M.S.V. conceived the concept. E.R. fabricated the QCL combs, integrated the devices with graphene, set up the transport and optical experiment, acquired and interpreted the experimental data. V.P. engineered the structure, performed the numerical simulations, set up and performed the TDS experiments and interpreted the experimental data. L.C. set up and performed the metrological characterization. L.C., A.S., F.C., R.E., and P.D.N. analyzed the FACE data. L.L., A.G.D., and E.H.L. performed the growth of the QCL structure. The paper was written by M.S.V. with support from E.R., V.P., and L.C. All authors contributed to the discussion and to the final paper. M.S.V. coordinated and supervised the project.

### Data Availability Statement

The data that support the findings of this study are available from the corresponding author upon reasonable request.

### Keywords

frequency combs, graphene, metrology, quantum cascade lasers, terahertz

Received: June 4, 2022

Revised: September 4, 2022

Published online: November 30, 2022

[1] T. W. Hänsch, *Rev. Mod. Phys.* **2006**, *78*, 1297.

[2] M. S. Vitiello, P. De Natale, *Adv. Quantum Technol.* **2022**, *5*, 2100082.

[3] L. Consolino, A. Taschin, P. Bartolini, S. Bartalini, P. Cancio, A. Tredicucci, H. E. Beere, D. A. Ritchie, R. Torre, M. S. Vitiello, P. De Natale, *Nat. Commun.* **2012**, *3*, 1040.



- [4] J. P. Epping, T. Hellwig, M. Hoekman, R. Mateman, A. Leinse, R. G. Heideman, A. Van Rees, P. J. M. Van Der Slot, C. J. Lee, C. Fallnich, K.-J. Boller, *Opt. Express* **2015**, *23*, 19596.
- [5] C. Liu, C. Zhu, M. Nie, H. Yang, C. Pei, *Opt. Express* **2022**, *30*, 14798.
- [6] W. Liang, A. A. Savchenkov, V. S. Ilchenko, D. Eliyahu, D. Seidel, A. B. Matsko, L. Maleki, *Opt. Lett.* **2014**, *39*, 2920.
- [7] M. Yu, Y. Okawachi, A. G. Griffith, N. Picqué, M. Lipson, A. L. Gaeta, *Nat. Commun.* **2018**, *9*, 1869.
- [8] A. Hugi, G. Villares, S. Blaser, H. C. Liu, J. Faist, *Nature* **2012**, *492*, 229.
- [9] D. Burghoff, T.-Y. Kao, N. Han, C. W. I. Chan, X. Cai, Y. Yang, D. J. Hayton, J.-R. Gao, J. L. Reno, Q. Hu, *Nat. Photonics* **2014**, *8*, 462.
- [10] J. B. Khurgin, Y. Dikmelik, A. Hugi, J. Faist, *Appl. Phys. Lett.* **2014**, *104*, 081118.
- [11] D. Burghoff, Y. Yang, D. J. Hayton, J.-R. Gao, J. L. Reno, Q. Hu, *Opt. Express* **2015**, *23*, 1190.
- [12] F. Cappelli, L. Consolino, G. Campo, I. Galli, D. Mazzotti, A. Campa, M. Siciliani De Cumis, P. Cancio Pastor, R. Eramo, M. Rösch, M. Beck, G. Scalari, J. Faist, P. De Natale, S. Bartalini, *Nat. Photonics* **2019**, *13*, 562.
- [13] N. Henry, D. Burghoff, Q. Hu, J. B. Khurgin, *IEEE J. Sel. Top. Quantum Electron.* **2019**, *25*, <https://doi.org/10.1109/JSTQE.2019.2929222>
- [14] D. Burghoff, Y. Yang, J. L. Reno, Q. Hu, *Optica* **2016**, *3*, 1362.
- [15] P. Tzenov, D. Burghoff, Q. Hu, C. Jirauschek, *Opt. Express* **2016**, *24*, 23232.
- [16] D. Bachmann, M. Rösch, G. Scalari, M. Beck, J. Faist, K. Unterrainer, J. Darmo, *Appl. Phys. Lett.* **2016**, *109*, 221107.
- [17] F. Wang, H. Nong, T. Fobbe, V. Pistore, S. Houver, S. Markmann, N. Jukam, M. Amanti, C. Sirtori, S. Moumdji, R. Colombelli, L. Li, E. Linfield, G. Davies, J. Mangeney, J. Tignon, S. Dhillon, *Laser Photonics Rev.* **2017**, *11*, 1700013.
- [18] G. Villares, S. Riedi, J. Wolf, D. Kazakov, M. J. Süess, P. Jouy, M. Beck, J. Faist, *Optica* **2016**, *3*, 252.
- [19] F. P. Mezzapesa, V. Pistore, K. Garrasi, L. Li, A. G. Davies, E. H. Linfield, S. Dhillon, M. S. Vitiello, *Opt. Express* **2019**, *27*, 20231.
- [20] A. D. Gaspare, E. A. A. Pogna, L. Salemi, O. Balci, A. R. Cadore, S. M. Shinde, L. Li, C. Franco, A. G. Davies, E. H. Linfield, A. C. Ferrari, G. Scamarcio, M. S. Vitiello, *Adv. Funct. Mater.* **2021**, *31*, 2008039.
- [21] F. P. Mezzapesa, K. Garrasi, J. Schmidt, L. Salemi, V. Pistore, L. Li, A. G. Davies, E. H. Linfield, M. Riesch, C. Jirauschek, T. Carey, F. Torrisi, A. C. Ferrari, M. S. Vitiello, *ACS Photonics* **2020**, *7*, 3489.
- [22] A. Forrer, M. Franckić, D. Stark, T. Olariu, M. Beck, J. Faist, G. Scalari, *ACS Photonics* **2020**, *7*, 784.
- [23] Y. Yang, D. Burghoff, J. Reno, Q. Hu, *Opt. Lett.* **2017**, *42*, 3888.
- [24] M. Beiser, N. Opačak, J. Hillbrand, G. Strasser, B. Schwarz, *Opt. Lett.* **2021**, *46*, 3416.
- [25] C. G. Derntl, G. Scalari, D. Bachmann, M. Beck, J. Faist, K. Unterrainer, J. Darmo, *Appl. Phys. Lett.* **2018**, *113*, 181102.
- [26] P. Cavalieri, J. Freeman, K. Maussang, E. Strupiechonski, G. Xu, R. Colombelli, L. Li, A. G. Davies, E. H. Linfield, J. Tignon, S. S. Dhillon, *Appl. Phys. Lett.* **2013**, *102*, 221101.
- [27] N. Opačak, S. D. Cin, J. Hillbrand, B. Schwarz, *Phys. Rev. Lett.* **2021**, *127*, 093902.
- [28] H. Willenberg, G. H. Döhler, J. Faist, *Phys. Rev. B* **2003**, *67*, 085315.
- [29] R. Terazzi, T. Gresch, M. Giovannini, N. Hoyler, N. Sekine, J. Faist, *Nat. Phys.* **2007**, *3*, 329.
- [30] A. Gordon, C. Y. Wang, L. Diehl, F. X. Kärtner, A. Belyanin, D. Bour, S. Corzine, G. Höfler, H. C. Liu, H. Schneider, T. Maier, M. Troccoli, J. Faist, F. Capasso, *Phys. Rev. A* **2008**, *77*, 053804.
- [31] N. Opačak, B. Schwarz, *Phys. Rev. Lett.* **2019**, *123*, 243902.
- [32] D. Burghoff, *Optica* **2020**, *7*, 1781.
- [33] T. S. Mansuripur, C. Vernet, P. Chevalier, G. Aoust, B. Schwarz, F. Xie, C. Caneau, K. Lascola, C.-E. Zah, D. P. Caffey, T. Day, L. J. Missaggia, M. K. Connors, C. A. Wang, A. Belyanin, F. Capasso, *Phys. Rev. A* **2016**, *94*, 063807.
- [34] M. Wienold, L. Schrottke, M. Giehler, R. Hey, W. Anders, H. T. Grahn, *Electron. Lett.* **2009**, *45*, 1030.
- [35] K. Garrasi, F. P. Mezzapesa, L. Salemi, L. Li, L. Consolino, S. Bartalini, P. De Natale, A. G. Davies, E. H. Linfield, M. S. Vitiello, *ACS Photonics* **2019**, *6*, 73.
- [36] R. E. Glover, M. Tinkham, *Phys. Rev.* **1957**, *108*, 243.
- [37] M. Brandstetter, M. Krall, C. Deutsch, H. Detz, A. M. Andrews, W. Schrenk, G. Strasser, K. Unterrainer, *Appl. Phys. Lett.* **2013**, *102*, 231121.
- [38] S. Kohen, B. S. Williams, Q. Hu, *J. Appl. Phys.* **2005**, *97*, 053106.
- [39] J. Kröll, J. Darmo, K. Unterrainer, *Opt. Express* **2007**, *15*, 6552.
- [40] R. Rungsaawang, N. Jukam, J. Maysonnave, P. Cavalieri, J. Madéo, D. Oustinov, S. S. Dhillon, J. Tignon, P. Gellie, C. Sirtori, S. Barbieri, H. E. Beere, D. A. Ritchie, *Appl. Phys. Lett.* **2011**, *98*, 101102.
- [41] J. Xu, J. M. Hensley, D. B. Fenner, R. P. Green, L. Mahler, A. Tredicucci, M. G. Allen, F. Beltram, H. E. Beere, D. A. Ritchie, *Appl. Phys. Lett.* **2007**, *91*, 121104.
- [42] P. R. Whelan, Q. Shen, B. Zhou, I. G. Serrano, M. V. Kamalakar, D. M. A. Mackenzie, J. Ji, D. Huang, H. Shi, D. Luo, M. Wang, R. S. Ruoff, A.-P. Jauho, P. U. Jepsen, P. B. G. Gilg, J. M. Caridad, *2D Mater.* **2020**, *7*, 035009.
- [43] H. A. Hafez, S. Kovalev, K. J. Tielrooij, M. Bonn, M. Gensch, D. Turchinovich, *Adv. Opt. Mater.* **2020**, *8*, 1900771.
- [44] R. A. Khabibullin, N. V. Shchavruk, D. S. Ponomarev, D. V. Ushakov, A. A. Afonenko, O. Y. Volkov, V. V. Pavlovskiy, A. A. Dubinov, *EPJ Web Conf.* **2018**, *195*, 04002.
- [45] C. A. Zaugg, Z. Sun, V. J. Wittwer, D. Popa, S. Milana, T. S. Kulmala, R. S. Sundaram, M. Mangold, O. D. Sieber, M. Golling, Y. Lee, J. H. Ahn, A. C. Ferrari, U. Keller, *Opt. Express* **2013**, *21*, 31548.
- [46] V. Bianchi, T. Carey, L. Viti, L. Li, E. H. Linfield, A. G. Davies, A. Tredicucci, D. Yoon, P. G. Karagiannidis, L. Lombardi, F. Tomarchio, A. C. Ferrari, F. Torrisi, M. S. Vitiello, *Nat. Commun.* **2017**, *8*, 15763.
- [47] F. Bianco, V. Miseikis, D. Convertino, J.-H. Xu, F. Castellano, H. E. Beere, D. A. Ritchie, M. S. Vitiello, A. Tredicucci, C. Coletti, *Opt. Express* **2015**, *23*, 11632.
- [48] L. Consolino, M. Nafa, F. Cappelli, K. Garrasi, F. P. Mezzapesa, L. Li, A. G. Davies, E. H. Linfield, M. S. Vitiello, P. De Natale, S. Bartalini, *Nat. Commun.* **2019**, *10*, 2938.
- [49] L. Consolino, M. Nafa, M. De Regis, F. Cappelli, K. Garrasi, F. P. Mezzapesa, L. Li, A. G. Davies, E. H. Linfield, M. S. Vitiello, S. Bartalini, P. De Natale, *Commun. Phys.* **2020**, *3*, 1.
- [50] M. DeRegis, F. Cappelli, L. Consolino, P. De Natale, R. Eramo, *Phys. Rev. A* **2021**, *104*, 063515.
- [51] G. Goertzel, *Am. Math. Mon.* **1958**, *65*, 34.
- [52] M. Singleton, P. Jouy, M. Beck, J. Faist, *Optica* **2018**, *5*, 948.
- [53] M. S. Vitiello, L. Consolino, M. Inguscio, P. D. Natale, *Nanophotonics* **2021**, *10*, 187.
- [54] V. Pistore, H. Nong, P.-B. Vigneron, K. Garrasi, S. Houver, L. Li, A. Giles Davies, E. H. Linfield, J. Tignon, J. Mangeney, R. Colombelli, M. S. Vitiello, S. S. Dhillon, *Nat. Commun.* **2021**, *12*, 1427.
- [55] R. Holzwarth, T. Udem, T. W. Hänsch, J. C. Knight, W. J. Wadsworth, P. St. J. Russell, *Phys. Rev. Lett.* **2000**, *85*, 2264.